



Cite this: RSC Adv., 2020, 10, 23829

 Received 26th May 2020
 Accepted 15th June 2020

 DOI: 10.1039/d0ra04641h
rsc.li/rsc-advances

Passivation by pyridine-induced PbI_2 in methylammonium lead iodide perovskites†

 Andre Cook, ^{ab} Timothy W. Jones,^b Jacob Tse-Wei Wang, ^b Hua Li,^c Rob Atkin, ^c Noel W. Duffy, ^d Scott W. Donne ^a and Gregory J. Wilson ^{*b}

Defects at discontinuities of the perovskite lattice limit the performance of the perovskite solar cell (PSC). Lead iodide (PbI_2) and pyridine have been shown to passivate these defects. We treat methylammonium lead iodide (MAPbI_3) films with pyridine solutions to investigate the effects of the two passivators. By comparing confocal fluorescence microscopy (CFM) images at 405 nm excitation and then at 559 nm excitation we demonstrate the pyridine treatment passivates and forms PbI_2 crystallites which cause additional passivation.

Introduction

The Perovskite Solar Cell (PSC) has rapidly become one of the leading thin-film solar technologies.^{1–8} Perovskite films grown using metal and organic cations combined with halide anions demonstrate strong light adsorbing properties with long charge carrier diffusion lengths.^{9–13} The ability to fabricate PSCs *via* solution processing from low-cost components, for example methylammonium lead iodide (MAPbI_3), that achieve light-to-electrical power conversion efficiencies (PCE) approaching that of commercial silicon has spurred a tremendous research effort.^{14–18} With laboratory scale PCE reaching 25.2% and perovskite on silicon tandems reaching 29.1% (ref. 19) research is moving into scaling-up fabrication and improving longevity.^{20,21} Defect reduction *via* surface passivation treatments of the perovskite layer is one of many avenues for improving performance and longevity.

Perovskite surfaces have a high density of Shockley–Read–Hall (SRH) traps,^{9,22–24} shown *via* the way charge carrier recombination rates increase with increased excitation intensity.²⁵ For a bare perovskite film, SRH traps form non-radiative recombination centers reducing the measured photoluminescence (PL), and ultimately device performance. These traps are theorized to be a result of ion vacancies at the edges of the perovskite lattice, in particular halide vacancies, resulting in under-coordinated lead cations.²⁶ Polar molecules can be used to balance the vacancies at the interface, passivating the trap.^{26,27} Pyridine, being a simple Lewis base, has become the focus of many PSC

studies, showing the ability to increase PL intensity and lifetime.^{23,24,26,28–30} Initial work into pyridine showed treated devices increased in performance from 13.1 to 16.5%.²⁶ Pyridine treatment has also been shown to reduce the heterogeneity between perovskite grains as observed in PL microscopy.²³ However lead iodide (PbI_2) is soluble in pyridine,²⁸ so to avoid destroying the film during the passivation treatment dilution of pyridine with an perovskite-inert solvent such as chlorobenzene or flash-treating the film with pyridine vapor is necessary.^{26,28} Despite the dilution, these methods have been shown to cause morphological changes in the film, indicating an effect beyond surface passivation.^{23,28} Films rich in PbI_2 have been reported by multiple research groups to show increased PL lifetimes, suggesting a passivation effect.^{31–34} Chen *et al.*³¹ used scanning Kelvin probe microscopy (SKPM) to show the contrast in surface potential between grains and grain boundaries is reduced upon annealing, attributed to increased PbI_2 at the boundaries post annealing.³¹ Definitive identification of PbI_2 regions within the perovskite film remained a hurdle, with most groups using XRD to identify the presence of PbI_2 within the film yet being unable to locate it specifically.^{31–33} Chen *et al.*³⁴ used confocal fluorescence microscopy (CFM) to identify PbI_2 grains within a perovskite film *via* the 510 nm PL peak. The PbI_2 rich regions were also shown to have longer PL lifetimes, indicating a passivation effect. However, the PbI_2 rich regions were perovskite-deficient so these PL decays were from low PL intensity regions.

Comparison of passivation by PbI_2 at different excitation wavelengths has begun to reveal more information. Argon-ion bombardment was used to induce a surface PbI_2 layer on MAPbI_3 films by Ren *et al.*,³⁵ these films showed an increase in photoconductivity at 532 nm excitation and a greater increase at 405 nm excitation, attributed to the high-energy photons being able to excite deeper energy levels.

Merdasa *et al.*³⁶ looked at photodegradation induced PbI_2 and evaporated PbI_2 on MAPbI_3 films, time-resolved

^aUniversity of Newcastle, Callaghan, NSW 2308, Australia

^bCSIRO Energy Centre, Mayfield West, NSW 2304, Australia. E-mail: Gregory.Wilson@csiro.au

^cSchool of Molecular Sciences, The University of Western Australia, WA 6009, Australia

^dCSIRO Energy Clayton Laboratories, Clayton, Vic 3169, Australia

† Electronic supplementary information (ESI) available. See DOI: 10.1039/d0ra04641h



photoluminescence (TRPL) at 450 nm which indicated radiative recombination at the PbI_2 – MAPbI_3 interface from charge carriers generated in the PbI_2 , which was not observed at 780 nm excitation.³⁶ Charge carrier migration from the PbI_2 could also explain the increased photoconductivity for Ren *et al.*³⁵ The combination of these studies shows a pronounced passivation effect by PbI_2 , with important interactions at the PbI_2 – MAPbI_3 interface which are dependent on excitation wavelength.

In this communication, we use atomic force microscopy (AFM) and confocal fluorescence microscopy (CFM) to probe the structure–performance characteristics of pyridine-treated MAPbI_3 perovskite films. From CFM imaging at different excitation wavelengths, we show that PbI_2 forms on, and passivates, the surface of the perovskite film as a result of the pyridine treatment.

Method

Methyl ammonium lead iodide (MAPbI_3 , perovskite) thin-films were fabricated using the procedure from Bai *et al.*³⁹ Methylammonium iodide (Greatcell Solar), 0.159 g mL^{-1} and lead iodide (TCI), 0.461 g mL^{-1} were dissolved in 9 : 1 (v/v) dimethylformamide : dimethylsulfoxide and spin coated in a nitrogen atmosphere onto plasma cleaned FTO substrate (4 cm^2 – 2 \times 2 cm) slides on a setting of 1000 rpm for 10 s and 4000 rpm for 20 s. 200 μL toluene antisolvent was added 10 s into the second step. The spin coated slides were then dried for 2 minutes in a nitrogen atmosphere and annealed for 10 minutes at 90 °C. Pyridine solution treatment was performed using a range of dilutions of pyridine in chlorobenzene, 1 mM, 10 mM, 100 mM and 1 M. 300 μL of the treatment solution was dispensed onto the 4 cm^2 perovskite sample with a 30 s dwell time and spun at 1000 rpm for 10 s in an N_2 atmosphere. Samples were stored in a low humidity light sealed box for transport and testing. Photoluminescence spectra were recorded on the samples on glass using a Cary Eclipse Fluorescence Spectrometer using a broad (10 nm) excitation centered at 532 nm. X-ray diffraction patterns were collected using a PANalytical Aeris benchtop X-ray diffractometer (Malvern) equipped with a Cu K α source operating at 40 kV and 15 mA. Data were collected in the range 7–65° 2θ with a step interval of \sim 0.043° 2θ . The perovskite films for XRD were deposited on FTO, utilizing the 26.6° 2θ peak for sample alignment and ensure consistent sample alignment.

Atomic force microscope (AFM) images were recorded using the samples on FTO in air using an Asylum Research Cypher scanning probe microscope. Tap300Al-G cantilevers from BudgetSensors were used for alternating contact imaging of the perovskite surface. Images were analyzed and exported using Gwyddion.³⁷ CPD was performed using a 2 V bias on the cantilever and a 10 nm tip to surface separation with minimal light to avoid photovoltage effects.

Confocal fluorescence microscopy was performed on the samples of glass using an Olympus Fluoview 1000. Images were recorded using the 60 \times oil objective, fluorescence spectra were taken with and without the microscope oil to verify the

microscope oil has no passivating effect. The excitation wavelengths of 405 nm and 559 nm were used with fluorescence being measured in two channels from 490–540 nm for the PbI_2 band and from 700–800 nm for the perovskite emission. Transmitted light was also recorded to identify non-adsorbing regions and holes in the film. Images were analyzed and exported using Fiji.³⁸

Results and discussion

Methylammonium lead iodide (MAPbI_3 , perovskite) thin-films were fabricated using the procedure from Bai *et al.*³⁹ Photoluminescence (PL) of the MAPbI_3 films with increasing pyridine concentration during treatment is shown in Fig. 1. The control MAPbI_3 film shows the typical PL signal centered at 770 nm.²⁶ The 1 mM treatment boosts the PL by 40%, whereas the 10 mM and 100 mM treatments cause 70% and 80% enhancement, respectively. The 10% difference in the 10 mM and 100 mM samples is within the expected variability of this experiment and is likely the maximum effective passivation that can be reached with this pyridine treatment. The PL enhancement is consistent with previous studies into pyridine treatments, where increased PL signal is attributed to passivation of the trap states or improved perovskite structure.^{23,24,26,28} The 1 M treated film (Fig. S1†) increased in PL over ten-fold, however also showed significant emission outside the 770 nm region. This large change in intensity and broad emission range for the 1 M treatment indicates large structural changes, which will be shown to be the case *via* XRD and AFM. Given that pyridine is a selective solvent for PbI_2 (ref. 28) the pyridine is likely extracting the PbI_2 out of the perovskite and pyridine is incorporated into the perovskite structure forming an amorphous network of 2D perovskite as seen *via* XRD by Jain *et al.*²⁸

XRD patterns, Fig. 2, for all samples show MAPbI_3 and FTO peaks. The PbI_2 peak at 12.7° 2θ is absent in the control sample and grows in intensity from 1 mM to 100 mM, showing the formation of PbI_2 from pyridine treatment. The 1 M treated sample has much lower intensity MAPbI_3 peaks, a lower PbI_2 peak than the other treated films and a new peak at 10° 2θ , all demonstrating decomposition of the perovskite structure and formation of new structures, which we would expect to cause

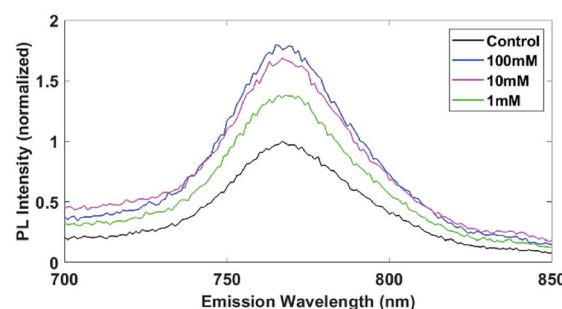


Fig. 1 PL enhancement with increasing pyridine treatment concentration on MAPbI_3 . Normalized to the peak height of the control sample. Performed at 532 nm excitation. 1 M treatment spectra is presented in the ESI.†



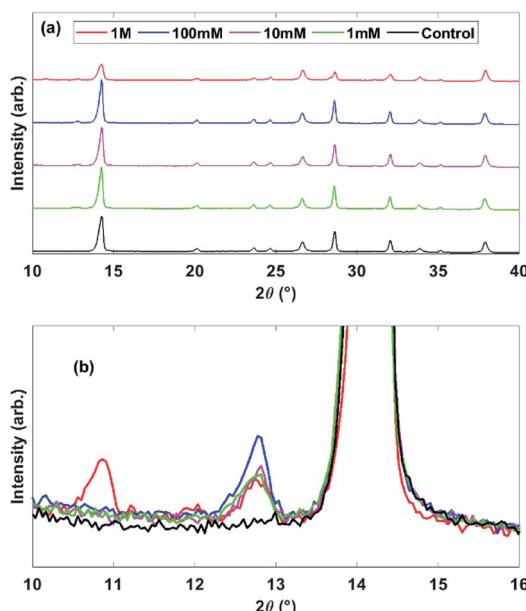


Fig. 2 XRD patterns for the pyridine treated MAPbI_3 samples on FTO, whole patterns for all samples (a) and an expanded region surrounding the 12.7° PbI_2 peak (b).

a lower device performance despite the high steady-state PL. This peak around 10° 2θ has been observed previously for a bleached pyridine-rich perovskite film to correspond to pyridine inclusions in the perovskite structure creating 2D perovskites.²⁸

To determine if passivation or restructuring is occurring, morphology and contact potential difference (CPD) images are recorded using AFM. Depicted in Fig. 3 are the control and the 100 mM pyridine treated films. We focus here on the 100 mM treated film as it shows the highest PL performance without the destruction of the perovskite film. Morphology images for the films show typical MAPbI_3 interlocking grains around 100–200 nm in size. The pyridine treatment causes no significant change in surface morphology until 100 mM, but drastic difference was observed in 1 M due to dissolution and recrystallization of the MAPbI_3 film (Fig. S3†). However the roughness data, Fig. 3, indicates the R_{rhs} is reduced by 50% after 1 mM pyridine introduction compared to the control, this reduction of R_{rhs} at intermediate pyridine concentrations may be attributed to the top surface reconstruction as similarly observed by Wang *et al.*, where the terrace/step-like defects on the crystal surface were removed and inferred from the reduced R_{rhs} .⁴¹ Furthermore, the control films have very different potential scales with pyridine treatment causing a 0.4 V drop in average CPD. Both images show low potential grains, which have been attributed to PbI_2 in other research,^{34,40} indicating the control film has a PbI_2 content below the detection limit of the XRD. The drop in CPD from passivation is shown in the plot of CPD *versus* treatment concentration in Fig. 3, where the control film has an average CPD (Av V) of 0.57 ± 0.05 V and the 1, 10 and 100 mM treated films are 0.13 ± 0.03 V. This drop in surface potential from passivation fits with the theory of halide vacancies causing

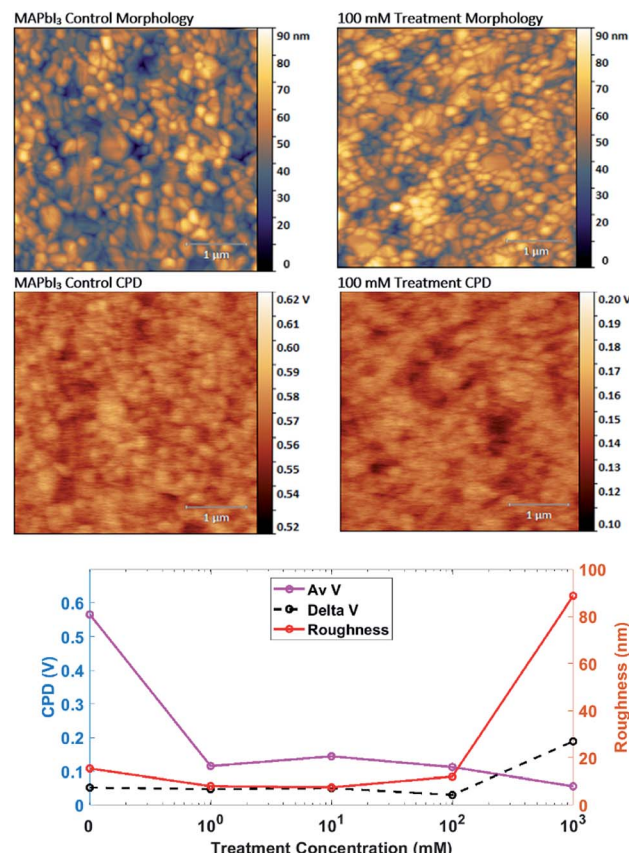


Fig. 3 Top – AFM morphology and CPD of control and 100 mM pyridine treated films. Note the difference in voltage scale between the CPD images. Bottom – roughness and CPD plots for the pyridine treated films. With the average surface CPD (Av V) and the difference between the highest and lowest potentials (delta V).

a positive charge which is counteracted by a Lewis base.²⁶ Though we note that the surface potential here is performed in low light conditions and so would still have a photovoltage contribution and we are measuring the potential difference the Pt coated AFM tip at 2 V bias. At 1 M pyridine treatment the average CPD drops to 0.06 V and the difference between the lowest potential and the highest potential on the image (delta V) increases from 0.05 V for the other films to 0.2 V, making it the only film to show a zero CPD at film pinholes through to the grounded FTO layer.

Enhancement in PL from pyridine Lewis base treatment therefore has contributions from Lewis base chemisorption and crystal restructuring. Depicted in Fig. 4 are CFM images of the 100 mM pyridine-treated MAPbI_3 film, which show the combined PL emission from perovskite and PbI_2 .³⁴ To investigate the passivation effect of pyridine and PbI_2 , excitation wavelengths of 405 nm and 559 nm are compared. Two channels are present in the 405 nm excitation images, the PbI_2 fluorescence band from 490–540 nm colored in yellow and the perovskite band from 700–800 nm in grey (see also emission spectra Fig. S2†). The PbI_2 emission band is not shown at 559 nm excitation as this wavelength is below the absorption of PbI_2 . The 405 nm excitation CFM image shows perovskite



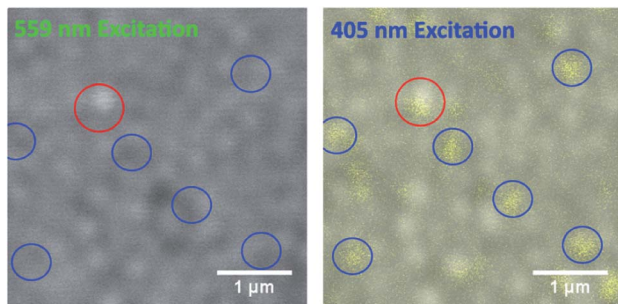


Fig. 4 CFM images of 100 mM pyridine treated MAPbI₃ at 559 nm excitation (left) and 405 nm excitation (right). The perovskite emission band 700–800 nm is in grey and the PbI₂ emission band 490–540 nm is in yellow. The blue highlighted region shows a PbI₂ grain in the film and the larger red highlighted region shows passivating PbI₂ on the film.

emission over most of the image sampled, and PbI₂ as grain sized regions of varying intensity. These grains are also visible in the control film (Fig. S5†) in agreement with the CPD images and suggesting a PbI₂ concentration lower than the detection limit of the XRD system or present in an amorphous layer. The 559 nm excitation image depicts only perovskite emission, with one high PL region highlighted by the red circle and multiple low PL regions in the blue circles. The highlighted low PL regions (blue circles) correspond to strong PbI₂ emission at 405 nm excitation so we attribute these regions to PbI₂ grains in the film. The red highlighted region has both enhanced PbI₂ emission in the 405 nm excitation and a higher perovskite PL emission at 559 nm excitation, indicating PbI₂ that has formed on, and is passivating, the surface of the perovskite film. These regions are not visible for the control, 1 mM or 10 mM treated films (Fig. S5†) indicating that the formation of this passivating PbI₂ results once a pyridine concentration threshold is passed. From this we identify the morphology changes seen by de Quilettes *et al.*²³ as pyridine induced PbI₂ and confirm results in previous work suggesting the passivation role of PbI₂.^{31,32,34,40} We note that the increased perovskite PL from the PbI₂ rich regions at 405 nm excitation could be due to charge carriers injected from the PbI₂ seen by Merdasa *et al.*,³⁶ however at 559 nm excitation the PbI₂ does not adsorb, confirming the passivation effect. The formation of PbI₂ may also explain the small increase in bulk PL intensity from 10 mM treatment to 100 mM, Fig. 1.

From these results, we demonstrate that pyridine is a selective solvent for PbI₂ more so than MAI, subsequently the pyridine/chlorobenzene solution partially dissolves the PbI₂ within the film, which then recrystallizes upon the removal of the solvent. These pyridine-induced PbI₂ crystals then passivate the traps at the perovskite surface, enhancing overall PL emission. We note that overall steady-state PL signal increase is a combined effect between the PbI₂ enhanced regions as well as the passivation of traps by the pyridine molecule across the whole film.

Conclusion

Through a combination of PL spectroscopy, XRD, AFM and CFM we demonstrate direct evidence of PbI₂ passivation on perovskite surfaces as a result of pyridine solution treatment. The pyridine treatment enhances the PL intensity in the perovskite band yet also induces an increase in the amount of PbI₂ shown *via* the XRD data. Through CFM imaging at 405 nm excitation, we identify PbI₂ grains *via* their fluorescence in the 510 nm band. Under 559 nm excitation, the PbI₂ covered regions fluoresce stronger than the surrounding regions, providing direct evidence for PbI₂ passivation of MAPbI₃ perovskite. This result provides crucial information on the role of PbI₂ within the perovskite film and the effect of pyridine treatments, allowing for further optimisation of such procedures for higher performance.

Conflicts of interest

There are no conflicts to declare.

Acknowledgements

A. C. acknowledges the University of Newcastle and the CSIRO Research Office for the provision of a PhD scholarship. J. T.-W. W. would like to thank the CSIRO Research Office for the support of his postdoctoral fellowship. G. J. W. acknowledges the CSIRO Research Office for the Julius Career Award in support of this study. This work was in part supported through funding from the Australian Renewable Energy Agency (ARENA) as part of ARENA's Emerging Renewables Program *via* grant P159394.

Notes and references

- 1 M. Habibi, F. Zabihi, M. R. Ahmadian-Yazdi and M. Eslamian, *Renewable Sustainable Energy Rev.*, 2016, **62**, 1012–1031.
- 2 M. Saliba, T. Matsui, J.-Y. Seo, K. Domanski, J.-P. Correa-Baena, M. K. Nazeeruddin, S. M. Zakeeruddin, W. Tress, A. Abate and A. Hagfeldt, *Energy Environ. Sci.*, 2016, **9**, 1989–1997.
- 3 D. Bi, W. Tress, M. I. Dar, P. Gao, J. Luo, C. Renievier, K. Schenk, A. Abate, F. Giordano and J.-P. C. Baena, *Sci. Adv.*, 2016, **2**, e1501170.
- 4 S. D. Stranks and H. J. Snaith, *Nat. Nanotechnol.*, 2015, **10**, 391–402.
- 5 J. H. Im, I. H. Jang, N. Pellet, M. Grätzel and N. G. Park, *Nat. Nanotechnol.*, 2014, **9**, 927–932.
- 6 D. Y. Liu and T. L. Kelly, *Nat. Photonics*, 2014, **8**, 133–138.
- 7 M. Grätzel, *Nat. Mater.*, 2014, **13**, 838–842.
- 8 H. J. Snaith, *J. Phys. Chem. Lett.*, 2013, **4**, 3623–3630.
- 9 R. J. Stewart, C. Grieco, A. V. Larsen, J. J. Maier and J. B. Asbury, *J. Phys. Chem. Lett.*, 2016, **7**, 1148–1153.
- 10 E. Edri, S. Kirmayer, S. Mukhopadhyay, K. Gartsman, G. Hodes and D. Cahen, *Nat. Commun.*, 2014, **5**, 3461.



11 C. S. Ponseca Jr, T. J. Savenije, M. Abdellah, K. Zheng, A. Yartsev, T. r. Pascher, T. Harlang, P. Chabera, T. Pullerits and A. Stepanov, *J. Am. Chem. Soc.*, 2014, **136**, 5189–5192.

12 C. Wehrenfennig, G. E. Eperon, M. B. Johnston, H. J. Snaith and L. M. Herz, *Adv. Mater.*, 2014, **26**, 1584–1589.

13 M. M. Lee, *Science*, 2012, **338**, 643–647.

14 S. Yang, Y. Wang, P. Liu, Y.-B. Cheng, H. J. Zhao and H. G. Yang, *Nat. Energy*, 2016, 15016.

15 H. Xiong, Y. Rui, Y. Li, Q. Zhang and H. Wang, *J. Mater. Chem. C*, 2016, **4**, 6848–6854.

16 B. Conings, *Adv. Mater.*, 2014, **26**, 2041–2046.

17 J. You, *ACS Nano*, 2014, **8**, 1674–1680.

18 A. Mei, *Science*, 2014, **345**, 295–298.

19 NREL, *Efficiency chart*, <https://www.nrel.gov/pv/assets/pdfs/best-research-cell-efficiencies-190416.pdf>, accessed 01-JUL-2019.

20 M. A. Green and A. W.-Y. Ho-Baillie, *ACS Energy Lett.*, 2017, **2**(4), 822–830.

21 J. Seo, J. H. Noh and S. I. Seok, *Acc. Chem. Res.*, 2016, **49**, 562–572.

22 J. Zhang, P. Wang, X. Huang, J. Xu, L. Wang, G. Yue, X. Lu, J. Liu, Z. Hu and Q. Wang, *RSC Adv.*, 2016, **6**, 9090–9095.

23 D. W. de Quilettes, S. M. Vorpahl, S. D. Stranks, H. Nagaoka, G. E. Eperon, M. E. Ziffer, H. J. Snaith and D. S. Ginger, *Science*, 2015, **348**, 683–686.

24 T. Tachikawa, I. Karimata and Y. Kobori, *J. Phys. Chem. Lett.*, 2015, **6**, 3195–3201.

25 Y. Yang, M. Yang, D. T. Moore, Y. Yan, E. M. Miller, K. Zhu and M. C. Beard, *Nat. Energy*, 2017, **2**, 16207.

26 N. K. Noel, A. Abate, S. D. Stranks, E. S. Parrott, V. M. Burlakov, A. Goriely and H. J. Snaith, *ACS Nano*, 2014, **8**, 9815–9821.

27 A. Abate, M. Saliba, D. J. Hollman, S. D. Stranks, K. Wojciechowski, R. Avolio, G. Grancini, A. Petrozza and H. J. Snaith, *Nano Lett.*, 2014, **14**, 3247–3254.

28 S. M. Jain, Z. Qiu, L. Häggman, M. Mirmohades, M. B. Johansson, T. Edvinsson and G. Boschloo, *Energy Environ. Sci.*, 2016, **9**, 3770–3782.

29 A. Ong, *Investigating the Effect of Pyridine Vapor Treatment on Perovskite Solar Cells*, SLAC National Accelerator Lab., Menlo Park, CA (United States), 2015.

30 H. Nagaoka, F. Ma, D. W. deQuilettes, S. M. Vorpahl, M. S. Glaz, A. E. Colbert, M. E. Ziffer and D. S. Ginger, *J. Phys. Chem. Lett.*, 2015, **6**, 669–675.

31 Q. Chen, H. Zhou, T.-B. Song, S. Luo, Z. Hong, H.-S. Duan, L. Dou, Y. Liu and Y. Yang, *Nano Lett.*, 2014, **14**, 4158–4163.

32 S. Wang, W. Dong, X. Fang, Q. Zhang, S. Zhou, Z. Deng, R. Tao, J. Shao, R. Xia and C. Song, *Nanoscale*, 2016, **8**, 6600–6608.

33 T. J. Jacobsson, J.-P. Correa-Baena, E. Halvani Anaraki, B. Philippe, S. D. Stranks, M. E. Bouduban, W. Tress, K. Schenk, J. Teuscher and J.-E. Moser, *J. Am. Chem. Soc.*, 2016, **138**, 10331–10343.

34 S. Chen, X. Wen, J. S. Yun, S. Huang, M. A. Green, N. J. Jeon, W. S. Yang, J. H. Noh, J. Seo and S. I. Seok, *ACS Appl. Mater. Interfaces*, 2017, **9**(7), 6072–6078.

35 L. Ren, M. Wang, S. Wang, H. M. Zeeshan, Y. Zhao, M. Li, H. Yan, C. Chen and K. Jin, *Thin Solid Films*, 2019, **685**, 360–365.

36 A. Merdasa, A. Kiligardidis, C. Rehermann, M. Abdi-Jalebi, J. Stöber, B. Louis, M. Gerhard, S. D. Stranks, E. L. Unger and I. G. Scheblykin, *ACS Energy Lett.*, 2019, **4**, 1370–1378.

37 D. Nečas and P. Klapetek, *Open Phys.*, 2012, **10**, 181–188.

38 J. Schindelin, I. Arganda-Carreras, E. Frise, V. Kaynig, M. Longair, T. Pietzsch, S. Preibisch, C. Rueden, S. Saalfeld and B. Schmid, *Nat. Methods*, 2012, **9**, 676–682.

39 J. T.-W. Wang, S. Bai, W. Sakai, J. Wang, F. Gao and H. J. Snaith, *Chem. Mater.*, 2016, **29**(1), 462–473.

40 Y. C. Kim, N. J. Jeon, J. H. Noh, W. S. Yang, J. Seo, J. S. Yun, A. Ho-Baillie, S. Huang, M. A. Green and J. Seidel, *Adv. Energy Mater.*, 2015, **6**(4), 15021.

41 J. T.-W. Wang, Z. Wang, S. Pathak, W. Zhang, D. W. deQuilettes, F. Wisnivesky-Rocca-Rivarola, J. Huang, P. K. Nayak, J. B. Patel, H. A. Mohd Yusof, Y. Vaynzof, R. Zhu, I. Ramirez, J. Zhang, C. Ducati, C. Grovenor, M. B. Johnston, D. S. Ginger, R. J. Nicholas and H. J. Snaith, *Energy Environ. Sci.*, 2016, **9**(9), 2892–2901.

